

## RESEARCH ARTICLE

# Intrinsic role of alkyl side chains in disorder, aggregates, and carrier mobility of nonfullerene acceptors for organic solar cells: A multiscale theoretical study

Rongkun Zhou<sup>1</sup> | Chao Li<sup>2</sup> | Zihao Wen<sup>3</sup> | Chen Zhang<sup>4</sup> | Yijie Shi<sup>1</sup> | Hao Hou<sup>1</sup> |  
Xiaoqing Chen<sup>5</sup> | Qian Kang<sup>5</sup> | Yongzhe Zhang<sup>5</sup> | Hui Yan<sup>1</sup> | Han Yu<sup>2</sup> |  
Yi Zhao<sup>3</sup>  | Zilong Zheng<sup>1</sup>  | He Yan<sup>2</sup>

<sup>1</sup>College of Materials Science and Engineering, Beijing University of Technology, Beijing, China

<sup>2</sup>Department of Chemistry, Clear Water Bay, Hong Kong University of Science and Technology, Hong Kong, China

<sup>3</sup>College of Chemistry and Chemical Engineering, Xiamen University, Xiamen, China

<sup>4</sup>Department of Computing, The Hong Kong Polytechnic University, Hong Kong, China

<sup>5</sup>Faculty of Information Technology, Beijing University of Technology, Beijing, China

## Correspondence

Zilong Zheng, College of Materials Science and Engineering, Beijing University of Technology, Beijing 100124, China.  
Email: zilong.zheng@bjut.edu.cn

## Funding information

National Natural Science Foundation of China, Grant/Award Numbers: 52073005, 22033006, 62034001; Beijing Municipal Natural Science Foundation, Grant/Award Number: JQ23020

## Abstract

Modifications to the alkyl side chains of Y6-type nonfullerene acceptors (NFAs) continuously break through the organic solar cells (OSCs) efficiency by enhancing electron mobility. However, the role of side chains in molecular aggregation and charge transport across different aggregates remains unclear. By employing a multiscale approach in combination with density functional theory (DFT), molecular dynamics (MD) simulations, and kinetic Monte Carlo (KMC), we addressed the issue of how side chains impact molecular aggregation, energy disorder, and the formation of near-macroscopic ( $\sim 0.3 \mu\text{m}$ ) conductive network, which are critical for boosting electron mobility. Specifically, the side-chain structure greatly influences the un-conjugated enveloping effect on backbones within aggregates. The effect diminishes with longer linear side chains and is further minimized by using branched side chains. Though static energy disorder increased, the improved connectivity of the conductive network led to a notable increase in electron mobility (from  $2.4 \times 10^{-4}$  to  $3.9 \times 10^{-4} \text{ cm}^2 \cdot \text{V}^{-1} \cdot \text{s}^{-1}$ ). The findings offer insight into controlling molecular aggregation via alkyl side chains, which helps to further unlock the potential of Y6-type NFAs.

## KEYWORDS

acceptors, aggregates, carrier mobility, conductive network, organic solar cells

## 1 | INTRODUCTION

Organic solar cells (OSCs) are increasingly considered a promising contender in the next-generation solar technologies.<sup>[1–4]</sup> Rapid development has been made with nonfullerene acceptors (NFAs) blended with polymer donors, propelling OSCs to impressive power conversion efficiencies that now exceed 20% using a Y6-type acceptor.<sup>[5–7]</sup> Extensive molecular design efforts, both theoretical and experimental, have been focused on optimizing both donor and acceptor materials, fine-tuning their electronic properties, and ensuring favorable energy level alignment.<sup>[8–15]</sup> However, challenges related to carrier mobility persist and impede further application of OSCs, owing to the low carrier mobility limits the short-circuit current ( $J_{\text{SC}}$ ) and fill factor of

OSC devices.<sup>[16]</sup> The morphology of the active layer plays a significant role in charge transport properties,<sup>[17–20]</sup> and the alkyl side-chain engineering of NFAs has emerged as a critical strategy for controlling this morphology.<sup>[21–29]</sup> Therefore, understanding and optimizing the morphology is essential for OSC performance improvement in terms of carrier mobility and device efficiency.

Following charge separation at the electron donors/acceptor (D/A) interface, the charge conductive network is composed of interconnected acceptor domains for electron transport and donor domains for hole transport. Efficient charge transport relies on a robust transport framework of interconnected acceptor (and donor) domains<sup>[30]</sup> and a minimal disorder of electronic state energies.<sup>[31,32]</sup> Generally, the short  $\pi$ - $\pi$  stacking distances with large

This is an open access article under the terms of the [Creative Commons Attribution](https://creativecommons.org/licenses/by/4.0/) License, which permits use, distribution and reproduction in any medium, provided the original work is properly cited.

© 2024 The Author(s). *Aggregate* published by SCUT, AIEI, and John Wiley & Sons Australia, Ltd.

intermolecular orbital overlaps result in high mobility via electron delocalization.<sup>[33–39]</sup> However, recent experimental observations seem to challenge traditional beliefs regarding achieving high carrier mobility. Varying the length of the linear alkyl side-chain on the thiophene ring of the BTP-4Cl backbone (a Y6-type acceptor)<sup>[21]</sup> alters the intermolecular stacking; starting from *n*-heptyl (BTP-eC7), *n*-nonyl (BTP-eC9), up to *n*-undecyl (BTP-eC11), despite BTP-eC7 film has the closest  $\pi$ - $\pi$  stacking distance and well-ordered mesoscopic structure, it has the worst mobility compared with the other longer side-chain counterparts (BTP-eC9 and BTP-eC11).<sup>[40]</sup> Replacing the linear side chains (undecyl) of Y6 with the branched chains (2-butyloctyl), known as L8-BO,<sup>[41]</sup> has proven to be a significant advancement in OSCs development. The seemingly straightforward modification enhances electron mobility, akin to adjusting the length of linear side chains. Despite resulting in a less-ordered molecular arrangement and weaker intermolecular electronic coupling, the switch from linear to branched side chains is crucial. Furthermore, shifting the branching position of the branched side chains on L8-BO from  $\beta$  to  $\gamma$  positions, referred to as L8-BO-X, has further electron mobility improvement.<sup>[42]</sup> These findings highlighted the profound impact of alkyl chain architecture on electron mobility in NFAs, suggesting that factors, other than the traditionally emphasized short  $\pi$ - $\pi$  distance and well-ordered molecular structures, potentially influence charge transport in organic materials. The structure-property correlations between these molecular structures and their effect on electron mobility are not yet fully understood, particularly in the small molecular organic semiconductor NFA domain. Uncovering the mechanism behind these seemingly contradicting physical phenomena could be crucial in refining the theoretical framework for how morphology impacts charge transport, thereby guiding the future optimization of OSCs for enhanced performance.

In this study, we employed a multiscale approach by combining density functional theory (DFT) calculations, molecular dynamics (MD) simulations, and kinetic Monte Carlo (KMC) method to unravel the intricate structure-property correlations between side-chain architecture and electron mobility in two series of Y6-type NFAs; while, ones were linear side-chain NFAs, including BTP-eC7, BTP-eC9, and BTP-eC11, with the length of linear side chains increasing from short to long; the others were branched side-chain NFAs, including Y6 as a reference molecule, along with L8-BO and L8-BO-X, which differ in branching positions, see Figure 1A. Our results indicated that for Y6-type NFAs, simply enhancing structural order and reducing stacking distance might not effectively improve electron mobility without ensuring an underlying well-connected charge transport framework. We discovered that the continuity of conductive network is primarily influenced by the aggregate configurations in NFA domains. The conjugated backbones within certain aggregates can be strongly enveloped by alkyl side chains, resulting in a notable decrease in connectivity within electron transport frameworks. Therefore, one promising approach for boosting carrier mobility lies in diminishing the distribution of such densely enveloped aggregates. Both extending linear side-chains or employing branched ones can facilitate the transformation of these aggregates to those with weak side-chain enveloping effects and modulate the solubility of NFA molecules, thereby enhancing electron mobility. These findings highlight potential strategies for molecular

engineering to advance the development of high-performance OSC materials.

## 2 | IMPACT OF SIDE CHAINS ON MOLECULAR STACKING MORPHOLOGY

The micromorphologies of NFA films were exported from MD equilibrium structures. The as-cast NFA films were formed from preaggregation in solution, driven by the van der Waals forces between adjacent conjugated NFAs.<sup>[43]</sup> The molecular assembly during solution processing significantly shaped the resulting film morphology, making extensive equilibration simulations pivotal for capturing solvent effects and reliable solid-state morphology. Figure S1 illustrates the number of molecular pairs formation throughout the chloroform (CF) solution process, reaching equilibrium following 200 ns MD simulations. The NFA dimers were classified into five types of stacking mode: C-, S-, S'-, Y'-, and Y-type by an agglomerative clustering algorithm (Figure S2). Figure 1B,C reveal the impact of linear side-chain length and branching position on the proportions of the five stacking modes. Y-type stacking, which boasted higher binding energy than the other modes, see Figure S3, dominated intermolecular configurations. As increasing linear side-chain lengths, the Y-type proportion decreased by approximately 10%, while the fraction of Y'-type rose from 22% to 27%. This is attributed to the enhanced solubility of NFAs with longer side chains, see Table S1, which dispersed Y-type stacking in solution, transitioning into structurally similar but energetically less stable Y'-type, see Figure S3. Treating BTP-eC7 films with high solubility CB solvent, yielded comparable changes in dimer distributions to those caused by longer linear side-chains, see Figure S8. Substituting linear (Y6) with branched side chains (L8-BO and L8-BO-X) leads to a nearly unchanged or even decreased solubility (Table S1 and Figure S12). However, the content of Y-type stacking is more significantly reduced by 14% to 17% (Figure 1C), considering the decreased potential energy differences between Y-type dimers and other stacking dimers (Figure S4). The transition from Y-type to Y'-type stacking can also be observed in the single-crystal structures of Y6 and L8-BO.<sup>[41]</sup>

Similar to the X-ray diffraction profile, the radial distribution function (RDF,  $g(r)$ ) could provide the distribution as a function of intermolecular distance, and the strong peaks indicate certain molecular intervals frequently present in the structure. Based on 500 snapshots from the trajectory in MD simulations, the first, second, and third D-D stacking RDF peaks for BTP-eC7 are sharper compared with those of BTP-eC9 and BTP-eC11 (Figure 1D). These peaks correspond to Y-type dimers, Y-type trimers, and Y-type tetramers, respectively, as the D-D stacking distances of these structures (Figure S18) align with the positions of the peaks in the  $g_{D-D}(r)$ . Therefore, BTP-eC7 has a tendency to form Y-type aggregates, including Y-type trimers and Y-type tetramers. BTP-eC7 presented a distinct RDF peak at 11.0 Å, because of the high density of Y-type tetramers. The peak aligns with the distance observed at 11.5 Å in the out-of-plane direction in previous grazing incidence wide-angle X-ray scattering (GIWAXS) measurement.<sup>[40]</sup> In contrast, both BTP-eC9 and BTP-eC11 with longer linear side chains, scarcely formed such aggregates in MD simulations or observed in GIWAXS characterization. Compared with Y6 with linear side chains,

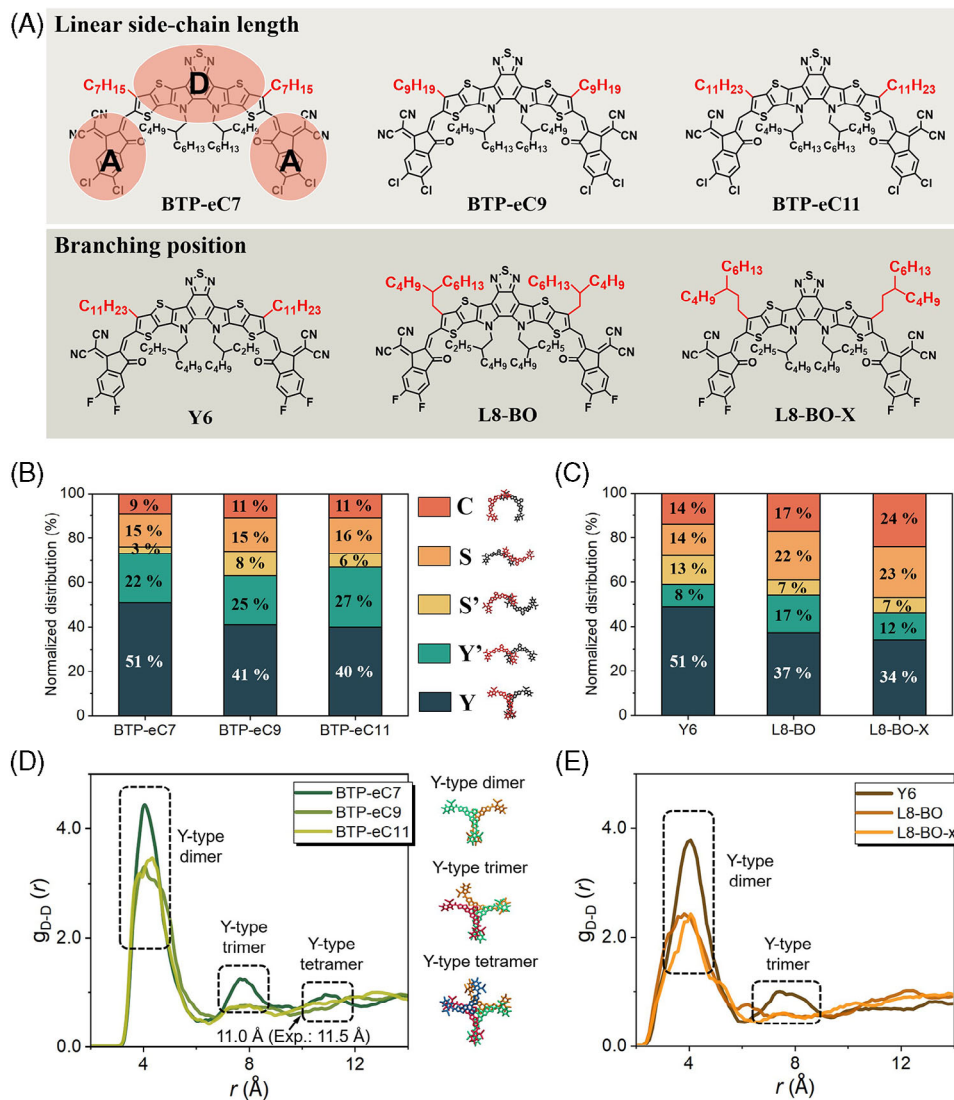


**FIGURE 1** The impact of side-chain on molecular stacking distributions. (A) Molecular structures of linear side-chain NFAs, including BTP-eC7, BTP-eC9, BTP-eC11, as well as, branched side-chain NFAs, for instance, Y6, L8-BO, L8-BO-X. The acceptor and donor moieties (denote as A and D, respectively) were marked on the A-D-A backbone of NFA. The distributions of five dimer stacking structures, (C-, S-, S'-, Y'-, and Y-type) for (B) linear and (C) branched side-chain NFAs. The radial distribution function  $g(r)$  between donor moieties as a function of stacking distance for (D) linear and (E) branched side-chain NFAs. The configurations of the peaks in (D) were Y-type dimer, trimer, and tetramer, respectively, in MD equilibrium.

both L8-BO and L8-BO-X with branched ones exhibited weaker D–D stacking peaks, correlating with a reduced density of Y-type stacking, see Figure 1E. The influence of linear side-chain length on A–A and D–A stacking in RDF was negligible (Figure S5). Introducing branched side chains increased S- and C-type content, sharpening the RDF peaks for D–A stacking (Figure S5), and suggesting a wider variety in molecular stacking.

These findings highlight that side-chain architecture can influence the stacking behavior of NFAs by regulating the solubility of NFA molecules and the binding energy of dimers, enhancing our understanding of the factors affecting their electronic properties.

### 3 | IMPACT OF SIDE CHAINS ON ENERGY DISORDERS

The electron transport rate is closely associated with the total energy disorder ( $\sigma_T$ ) of  $LUMO_{NFA}$ , which arises from

the contributions of both dynamic ( $\sigma_D$ ) and static disorders ( $\sigma_S$ ), expressed as  $\sigma_T^2 = \sigma_S^2 + \sigma_D^2$ .<sup>[44]</sup> Elevated levels of  $\sigma_T$  introduce additional energy barriers and scattering centers for charge carriers within materials, ultimately impeding carrier mobility.<sup>[45]</sup>  $\sigma_D$  stems from temporal energy fluctuations due to molecular vibrations, affecting charge carrier energies variably over time.  $\sigma_S$  is caused by spatial inhomogeneities like diverse molecular orientations and defects, which create a heterogeneous energy landscape. Thus, understanding the impact of alkyl side-chain structure on energy disorder is critical. We investigated the influences of linear side-chain length and branching position on  $\sigma_T$ ,  $\sigma_D$ , and  $\sigma_S$ , respectively. Lengthening linear side-chain escalated the  $\sigma_T$ , see Figure 2A. The  $\sigma_T$  can be reflected by the Urbach energy, demarcating the tail width of the absorption coefficient curve at low photon energies.<sup>[46]</sup> Our calculations agreed well with the experimentally observed Urbach energy trends as a function of linear side-chain length,<sup>[40]</sup> and aligned with the previous experimental values of energy disorders (53~71 meV).<sup>[47,48]</sup>

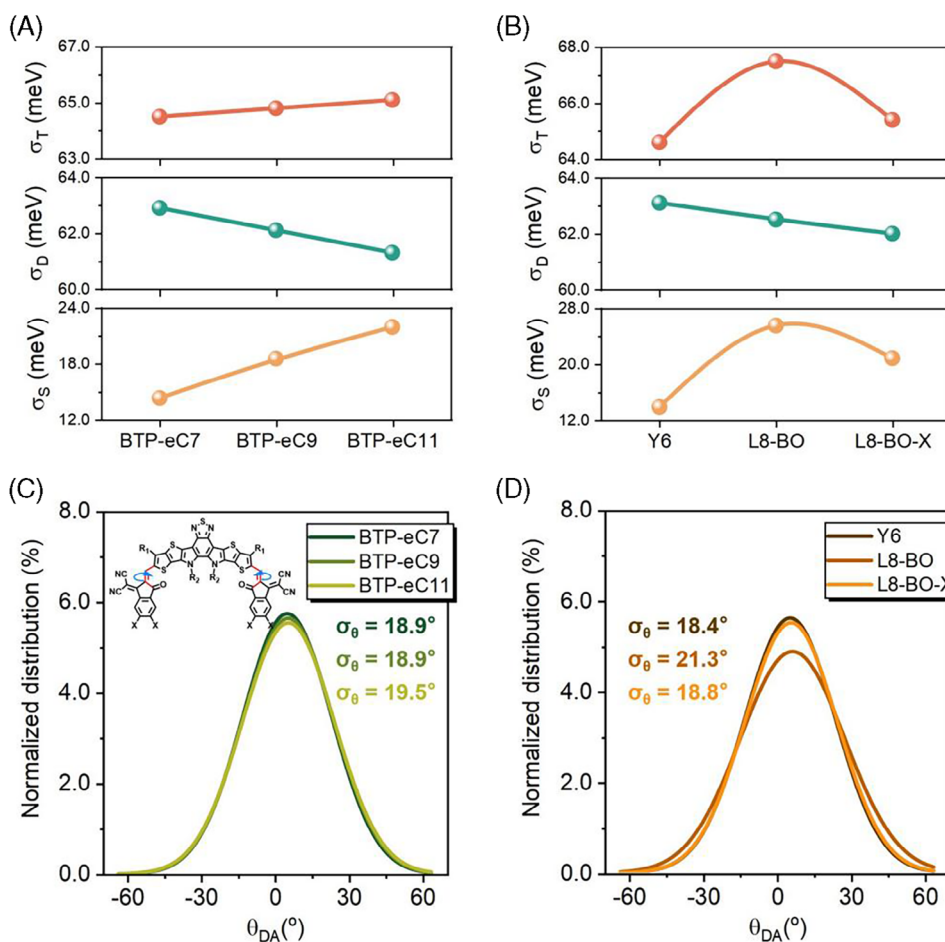


**FIGURE 2** NFAs LUMO energy disorders with linear (long and short) and branched alkyl side chains. LUMO energy total ( $\sigma_T$ ), dynamic ( $\sigma_D$ ), and static ( $\sigma_S$ ) disorders exported from MD simulations for (A) linear and (B) branched side-chain NFAs. Distributions ( $\theta_{DA}$ ) and disorder ( $\sigma_\theta$ ) of dihedral angle between donor (D) and acceptor (A) moieties in A-D-A backbone, for (C) linear and (D) branched side-chain NFAs.

Substituting the linear side-chain of Y6 with a branched one (L8-BO) resulted in a notable upsurge in  $\sigma_T$ . Interestingly, repositioning the branching position from the  $\beta$ -site to the  $\gamma$ -site (L8-BO-X) led to a reduction in the  $\sigma_T$ , see Figure 2B. It was found that the increase in carbon number within side chains slightly reduces the  $\sigma_D$ , as the added side-chain mass curtails the structure's thermal vibrations. Figure S13 illustrates this relationship for the six molecules. However, the elongation of linear side chains and the introduction of branched side chains lead to an increase in  $\sigma_T$ , primarily driven by a rise in  $\sigma_S$ , indicating the increasingly disordered molecular stacking.<sup>[49]</sup> Crucially, the  $\sigma_S$  originated from the dihedral angle disorder ( $\sigma_\theta$ ) between the D and A moieties, see Figure 2C,D. Both BTP-eC7 and Y6 exhibited low  $\sigma_S$  in linear and branched side-chain NFA groups, due to their dominant Y-type stacking that simplifies the stacking configurations.

We observed that the branching position in side chains significantly impacted on  $\sigma_\theta$ . Elevated  $\sigma_\theta$  in L8-BO results from branching site proximity to the conjugated backbone, engendering pronounced steric hindrance and a consequent rise in  $\sigma_S$ . Conversely, increasing the spacing between the branching site and the conjugated backbone, specifically shifting from the  $\beta$ -site to the  $\gamma$ -site (L8-BO-X), mitigated stacking steric hindrance and promoted charge transport.

## 4 | IMPACT OF AGGREGATES ON ELECTRON DISTRIBUTIONS

In amorphous NFA films, efficient charge transfer is facilitated by internally order-stacked aggregates. The influence on electron transport, however, arises at the multiple inter-aggregate boundaries. Besides, diverse molecular stacking architectures were associated with varying electron transfer rates, which creates a tortuous electron transport pathway. In order to consider these factors, instead of the traditional periodic lattice methodology, we conduct KMC simulations employing conductive network graphs transformed from MD-simulated NFA films; each molecule was represented as a node in KMC, with attributes including site energy and centroid coordinates of backbone; the edges denoted  $\pi$ - $\pi$  interactions between adjacent molecules. The density of electron distribution was then projected onto the centroid coordinates of molecules, representing the probability of electrons occurring across different film regions. Areas of high density signaled more extensive electron transport pathways and a greater number of atoms involved in  $\pi$ - $\pi$  stacking.

Y-type stacking, the predominant stacking mode in Y6-type acceptor films (Figure 1B,C), significantly influences charge transport properties. We found that despite the strong LUMO-LUMO coupling demonstrated by these dimers

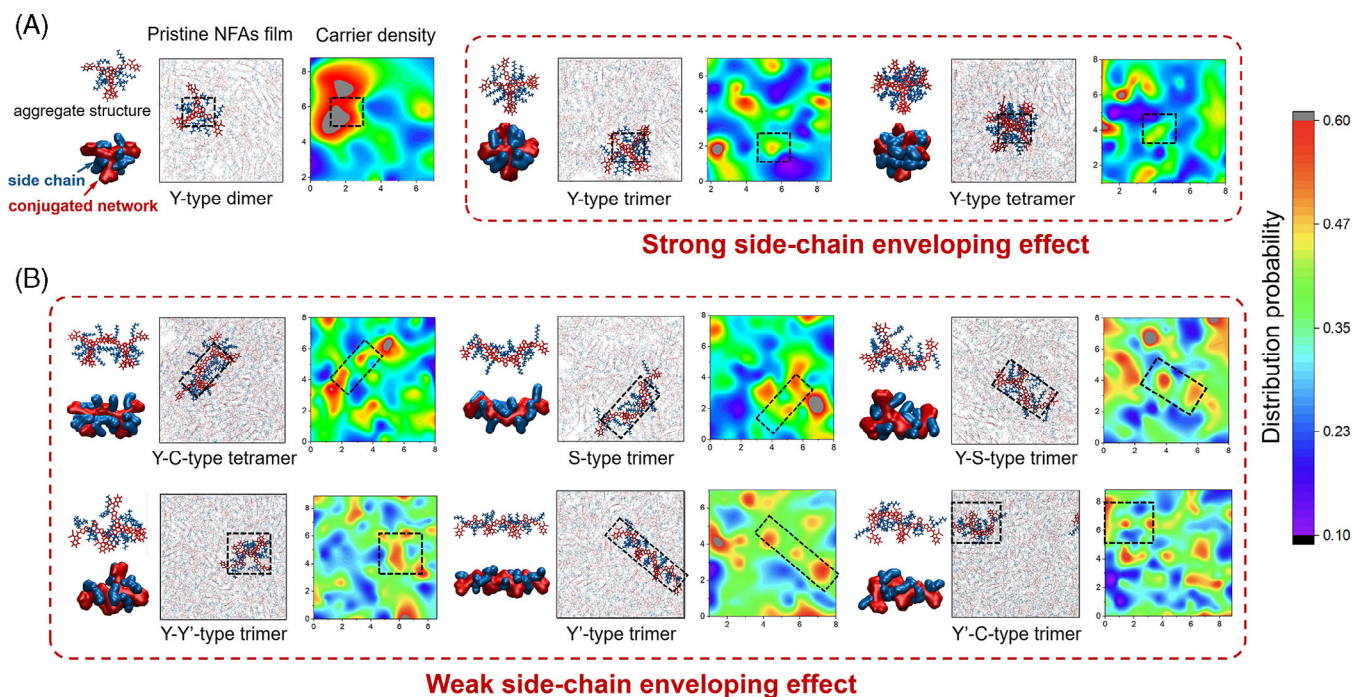


**FIGURE 3** Electron distributions in the dynamic process of electron transport within NFA aggregates. The stacking structures of (A) Y-type multimers (dimer, trimer, and tetramer) from BTP-eC7 and Y6, (B) the other multimers, including Y-C-, Y-Y'-, S-, Y', Y-S-, and Y'-C-types aggregations from BTP-eC9, BTP-eC11, L8-BO, and L8-BO-X, with electron distributions in the conductive networks.

(Figure S6), Y-type aggregate—multiple Y-type dimers clustered continuously together—acts as a barrier to electron transport. As shown in Figure 3A, as an increase in aggregation from Y-type dimer to trimer and then to tetramer, the conjugated backbone gradually being enveloped by alkyl side chains. This side-chain enveloping effect hinders further stacking interactions with adjacent molecules, leading to a gradual decrease in the density of electron distribution within Y-type aggregates. This is because the lateral extent of the Y-type aggregates remains approximately 3.1 nm even as the number of stacked molecules increases (Figure S14A). The limited spatial extension allows the conjugated backbone to be increasingly enveloped by the growing number of alkyl side chains. In contrast, aggregates with weak side-chain enveloping effects (Figure 3B), left the conjugated backbones relatively exposed due to substantial spatial extension (4.3~5.8 nm, Figure S14B), boosting stacking interface with proximal molecules. This promoted a high electron distribution density, thereby, aiding the establishment of a broad and cohesive conductive network.

## 5 | IMPACT OF CONDUCTIVE NETWORK ON CHARGE TRANSPORT

In order to understand the physical connection between side chain architecture and charge transport properties, we explored the diverse aggregates and the connectivity within conjugated networks in NFA films. As shown in Figure 4A,D, the linear side-chain length and the branching sites significantly influence the density of various aggregates. When extending linear side chains (BTP-eC9 and BTP-eC11) or employing branched ones (L8-BO and L8-BO-X), an increase in aggregate densities with a weaker side-

chain enveloping effect was observed compared with their reference samples, BTP-eC7 and Y6. Such modification stems from changes in the proportions of different stacking dimers, see Figure 1B,C.

The impact of alkyl side chains on the continuity of the conductive network is illustrated in Figure 4B,E. The conductive network is formed by the continuous stacking of molecular pairs that meet the  $\pi$ - $\pi$  stacking definition: at least 16 interacting atoms with interatomic distances smaller than 4 Å (Figure S17). The backbone envelopment by side chains in Y-type aggregates restricted the connectivity of the conductive network, giving rise to discrete localized order-stacking regions. Consequently, BTP-eC7 and Y6 exhibit small conductive network sizes for linear and branched side-chain series NFAs, respectively, due to high-density Y-type aggregates. Despite potential steric hindrance from branched side chains, they reduced the Y-type density, thus broadening and strengthening the conjugated networks. Besides, the various  $\pi$ - $\pi$  stacking distances were observed from 3.6 Å (in short side-chain NFAs) to 3.8 Å (in long side-chain NFAs), see Figure S11B in SI. The large  $\pi$ - $\pi$  stacking distances prompted by overly long linear side-chains of BTP-eC11 can reduce the connectivity of the conductive network, as shown in the expansive conjugated networks extracted from MD-simulated NFA films. While replacing linear side-chains with branched ones has a minimal impact on the  $\pi$ - $\pi$  stacking distances (Figure S11A in SI).

We performed KMC simulations to calculate the electron mobility. To mirror experimental film thicknesses for electron mobility measurements, we expanded the original MD-simulated equilibrium structures by a factor of 32, 16, and 8 in the X, Y, and Z directions, respectively, resulting in a mesoscopic film with a width of approximately 300 nm, composed of  $1.2 \times 10^7$  NFA molecules. Electron injection points were

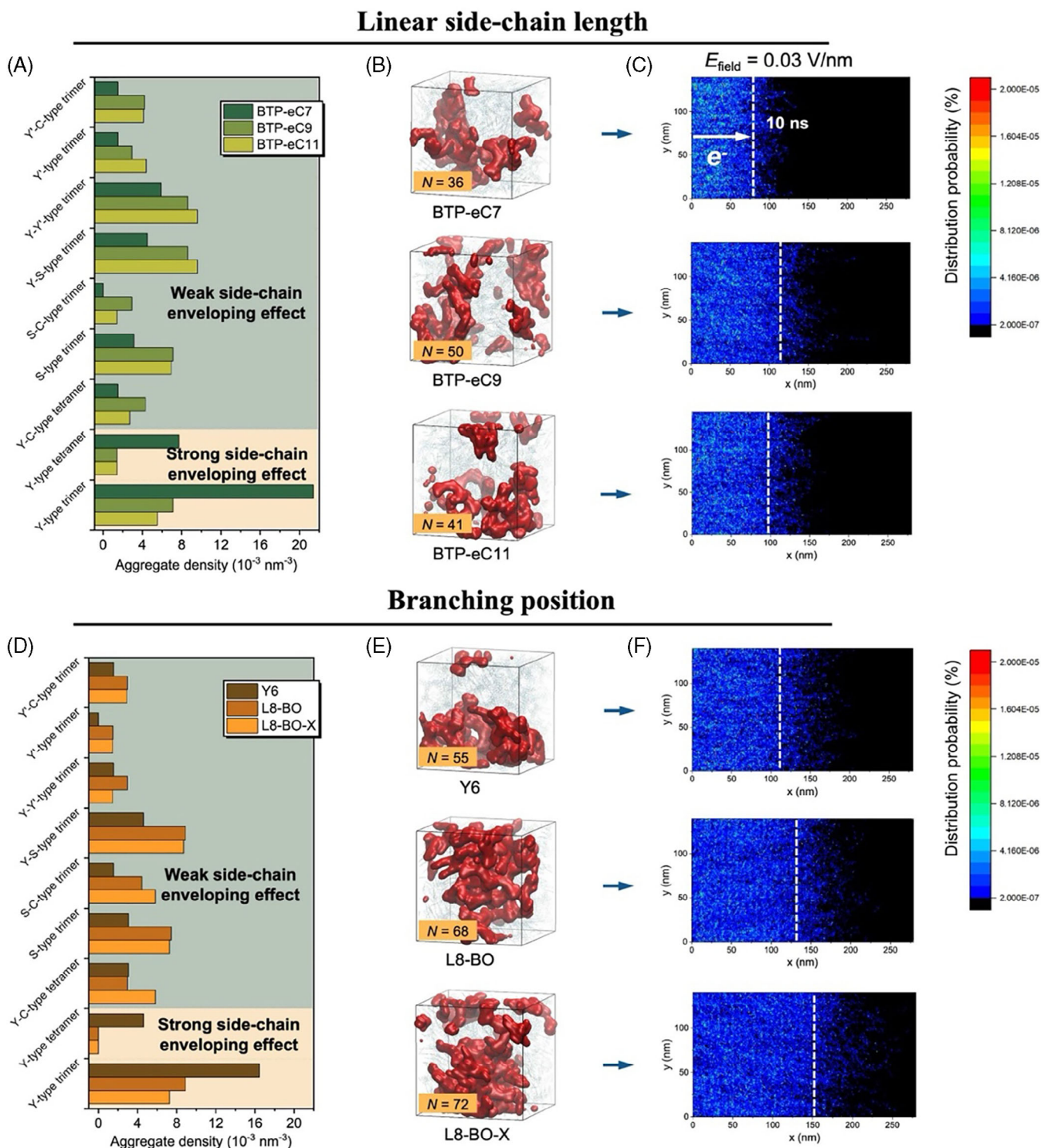


**FIGURE 4** Impact of stacking mode distributions on electron transport processes. The density of aggregates with weak and strong side-chain enveloping effect in (A) linear and (D) branched side-chain NFAs. The maximum molecular numbers ( $N$ ) in conjugated networks exported from MD equilibrium structures, for (B) linear and (E) branched side-chain NFAs. Electron transport in (C) linear and (F) branched side-chain NFAs, under an external electric field in 10 ns KMC simulations, within 300 nm mesoscopic structures expanded from MD-simulated equilibrium structures.

randomly assigned, and electron trajectories from at least 500 KMC simulations were superimposed for each NFA material. Under an applied electric field ( $\epsilon_x$ ) of 0.03 V/nm (a common value for experimental carrier mobility measurement) along the X-axis direction, as shown in Figure 4C,F, the average electron transfer distances highlighted the connectivity within NFA conductive networks. Constrained electron channels resulted in low electron mobilities, with theoretical upper

limits detailed in Table 1. The connectivity fundamentally influenced electron transport; despite resembling conductive networks sizes, L8-BO-X achieved higher electron mobility ( $\mu_{\text{L8-BO-X}} = 3.9 \times 10^{-4} \text{ cm}^2 \cdot \text{V}^{-1} \cdot \text{s}^{-1}$ ) than  $3.6 \times 10^{-4} \text{ cm}^2 \cdot \text{V}^{-1} \cdot \text{s}^{-1}$  of L8-BO, due to the lower static disorder in L8-BO-X, see Figure 2B. Our results were consistent with the previous experimental values, affirming the validity of the theoretical understanding, see Table 1.

**TABLE 1** The theoretical (Theo.) and experimental (Exp.) electron mobilities ( $\mu_e$ ) of NFAs with linear and branched side chains.

Side chain	NFAs	$\mu_e$ [ $10^{-4}$ cm <sup>2</sup> ·V <sup>-1</sup> ·s <sup>-1</sup> ]	
		Theo. <sup>a</sup>	Exp. <sup>b</sup>
Linear	BTP-eC7	2.4	1.3 <sup>[40]</sup>
	BTP-eC9	3.0	2.7 <sup>[40]</sup>
	BTP-eC11	2.9	2.5 <sup>[40]</sup>
Branche	Y6	3.4	4.5 <sup>[41]</sup>
	L8-BO	3.6	6.8 <sup>[41]</sup>
	L8-BO-X	3.9	8.2 <sup>[42]</sup>

<sup>a</sup>Calculated by the combination of MD and KMC approach.<sup>b</sup>Measured by the space-charge limited current (SCLC) method.

## 6 | CONCLUSION

In conclusion, our study implied that the cornerstone for high electron mobility is the establishment of a well-connected conjugated network with low energy disorder. Minimizing the prevalence of Y-type aggregates, wherein conjugated backbones are strongly enveloped by side chains, is essential for facilitating a well-connected conductive network. Increasing linear side-chain length was found to boost NFA solubility, promoting the transition from tightly shielded Y-type aggregates to ones that are less enveloped by side-chains, thereby enhancing electron mobility (from  $\mu_{\text{BTP-eC7}} = 2.4 \times 10^{-4}$  cm<sup>2</sup>·V<sup>-1</sup>·s<sup>-1</sup> to  $\mu_{\text{BTP-eC11}} = 2.9 \times 10^{-4}$  cm<sup>2</sup>·V<sup>-1</sup>·s<sup>-1</sup>). A more pronounced transition occurs upon replacing a linear side-chain with a branched one, lowering the binding energies of Y-type aggregates and enhancing electron mobility (from  $\mu_{\text{Y6}} = 3.4 \times 10^{-4}$  cm<sup>2</sup>·V<sup>-1</sup>·s<sup>-1</sup> to  $\mu_{\text{L8-BO}} = 3.6 \times 10^{-4}$  cm<sup>2</sup>·V<sup>-1</sup>·s<sup>-1</sup>) despite lower NFA solubility. This alteration was associated with a diversity of stacking arrangements and a consequent rise in static energy disorder. However, repositioning branching points further from the conjugate backbone allows for the retention of a robust conductive network alongside mitigation of static energy disorder, resulting in optimal electron mobility ( $\mu_{\text{L8-BO-X}} = 3.9 \times 10^{-4}$  cm<sup>2</sup>·V<sup>-1</sup>·s<sup>-1</sup>). These insights provide a fresh perspective for the molecular engineering of OSC materials, aiming to enhance carrier mobility through strategic control over aggregate formation and evolution. Furthermore, this work advanced our understanding of the role that morphology plays in charge transport within small-molecule organic semiconductors, laying the groundwork for future innovations in OSC technology.

### 6.1 | Calculation methods

#### 6.1.1 | Density functional theory calculations

All DFT calculations were performed at the turned- $\omega$ B97XD/6-31G(d) level via the Gaussian16 package.<sup>[50]</sup> A polarizable continuum model (PCM) with a dielectric constant of 3.5 (a representative value of organic semiconductor materials) was applied for the impact of the solid-state environment. The range separation parameter ( $\omega$ ) was optimized by minimizing the value of  $J(\omega)$  (Equation 1).<sup>[51–53]</sup>

$$J(\omega) = [\epsilon_{\text{HOMO}}(\omega) - \text{IP}(\omega)]^2 + [\epsilon_{\text{LUMO}}(\omega) - \text{EA}(\omega)]^2, \quad (1)$$

where  $\epsilon_{\text{HOMO}}(\omega)$  and  $\epsilon_{\text{LUMO}}(\omega)$  denote the energies of the highest occupied molecular orbital (HOMO) and the lowest unoccupied molecular orbital (LUMO), respectively. IP and EA represent the first ionization potential and electron affinity. The optimal  $\omega$  values for BTP-eC7, BTP-eC9, and BTP-eC11 were obtained as 0.0109 bohr<sup>-1</sup>.

#### 6.1.2 | Molecular dynamics simulations

The MD simulations were performed via the GROMACS (version 2018.4) software package.<sup>[54,55]</sup> A velocity-rescale thermostat was applied for the temperature, and a Berendsen thermostat was used to maintain a pressure of 1 atm. Periodic boundary conditions and the OPLS-AA (optimized potentials for liquid simulations of all atoms) force field<sup>[56,57]</sup> were employed. Particle mesh Ewald electrostatics were applied to calculate the long-range electrostatic interactions. The short-range electrostatic and van der Waals cutoff distances were set to 2 and 1.5 nm, respectively. The equilibrium bond lengths and angles for the NFAs and chloroform molecules were updated based on the DFT-optimized geometries. These ground-state structures exhibit no imaginary frequencies through vibrational frequency analysis. The dihedral potentials that dictate the planarity of the conjugated molecules were re-parameterized based on the DFT potential energy surfaces. The atomic partial charges were fitted using the restrained electrostatic potential method<sup>[58]</sup> via the Multiwfn (version 3.6) software package.<sup>[59]</sup>

The film morphologies of BTP-eC7, BTP-eC9, BTP-eC11, Y6, L8-BO, L8-BO-X were obtained as the following steps: (1) constructing a box containing 300 NFAs molecules and 20000 chloroform (CF) or chlorobenzene (CB) solvent molecules by randomly placing NFAs molecules into the solvent; (2) equilibrium of the NFAs-solvent mixed system was performed for 230 ns to balance the self-assembly process; (3) subsequently, we randomly removed 100 chloroform from the box in every 0.5 ns to simulate the solvent evaporation process; (4) as all the chloroform were removed, we carried out equilibration simulations at room temperature for 60 ns, then obtained the as-cast films.

#### 6.1.3 | Kinetic Monte Carlo simulations

In order to understand the physical connection between micromorphology and charge transport property, we performed KMC simulations based on the conductive networks exported from MD simulations. Given the carrier density in organic semiconductor materials is low, we only considered the distribution or transport of a single electron in the conducting network.

The site energy of NFAs film sites is assumed to have Gaussian distribution,  $g(E)$ , which could be derived from Equation (2).<sup>[60]</sup>

$$g(E) = \frac{1}{\sqrt{2\pi\sigma_T^2}} \exp\left(-\frac{E^2}{2\sigma_T^2}\right), \quad (2)$$

where  $\sigma_T$  represents the total energy disorder of LUMOs. The charge-transfer rates in the NFAs were estimated by the semiclassical Marcus Equation (3):<sup>[61]</sup>

$$k_{ij} = \frac{|V_{ij}|^2}{\hbar} \sqrt{\frac{\pi}{\lambda k_B T}} \exp\left(-\frac{(\lambda + \Delta G_{ij})^2}{4\lambda k_B T}\right), \quad (3)$$

where  $\hbar$  denotes the reduced Planck's constant;  $T$  is temperature and set to 300 K;  $V_{ij}$ ,  $\Delta G_{ij}$ , and  $\lambda$  denote electronic coupling, free energy of the electron-transfer reaction, and reorganization energy from site  $i$  to site  $j$ .

Following the separation of excitons into electrons and holes at the D/A interface, the electrons are mainly transported by hopping between LUMOs of the NFA molecules. The LUMO-LUMO ( $V_{L-L}$ ) couplings were calculated employing the fragment charge difference method<sup>[62]</sup> based on 350 pairs of adjacent molecules exported from the MD-simulated films. The Gaussian fits of the electronic coupling distribution corresponding to different ranges of atomic stacking numbers were summarized in Figure S10. The intramolecular reorganization energies ( $\lambda_{\text{int}}$ ) were calculated using the four-point method shown in Table S2. The intermolecular reorganization energy ( $\lambda_{\text{ext}}$ ) was set to 0.1 eV.<sup>[63,64]</sup>

The time evolution of the electron transport modeling system was described by the KMC algorithm. The charge transfer probability to another molecule was proportional to the charge transfer rate. The carrier residence time  $t_i$  on site  $i$  and the hopping direction  $k$  were calculated using Equations (4) and (5):<sup>[65–67]</sup>

$$t_i = -\frac{\ln(\xi_1)}{\sum_j v_{ij}}, \quad (4)$$

$$\sum_{j=1}^{k-1} v_{ij} < \xi_2 \sum_j v_{ij} \leq \sum_{j=1}^k v_{ij}, \quad (5)$$

where  $\xi_1$  and  $\xi_2$  are random numbers with a range of 0 to 1.

To determine the zero-field mobility, we repeated the single-electron KMC simulations (Figure S15) 10,000 times under different electric fields and obtained the relationships between mobility and electric field intensity (Figure S16). Based on the Poole-Frenkel behavior (Equation (6)):<sup>[60,68,69]</sup>

$$\mu = \mu_0 \exp\left(\beta\sqrt{F}\right), \quad (6)$$

where  $\mu$  is the field-dependent mobility;  $\mu_0$  is the zero-field mobility;  $\beta$  is the Poole-Frenkel factor; and  $F$  is the electric field strength. From the relationships, we derived the zero-field electron mobilities ( $\mu_0$ ) for the six Y6-series acceptor films.

#### 6.1.4 | The solvation-free energy of NFAs

In the solvation model based on the solute electron density model, the free energy of solvation can be defined as Equation (7):<sup>[70]</sup>

$$\Delta G_{\text{solv}} = (E_{\text{solv}} + G_{\text{ne}}) - E_{\text{gas}}, \quad (7)$$

where  $E_{\text{solv}}$  and  $E_{\text{gas}}$  are the electronic energies of the solute in the solvent and vacuum, respectively.  $G_{\text{ne}}$  is the non-electrostatic contribution, which includes the energies of solute-solvent intermolecular exchange, mutual repulsion, and dispersion attraction interaction.

#### ACKNOWLEDGEMENTS

This work was financially supported by the National Natural Science Foundation of China (NSFC, grants 52073005, 22033006, and 62034001) and the Beijing Municipal Natural Science Foundation (BNSF, grant JQ23020). The authors also acknowledge the financial support from the Key Laboratory of Advanced Functional Materials, the Education Ministry of China, and the supercomputer center of the Institute of Advanced Energy Materials and Devices in BJUT.

#### CONFLICT OF INTEREST STATEMENT

The authors declare no conflict of interest.

#### DATA AVAILABILITY STATEMENT

The data that support the findings of this study are available in the Supporting Information of this article.

#### ORCID

Yi Zhao  <https://orcid.org/0000-0003-1711-4250>

Zilong Zheng  <https://orcid.org/0000-0003-4310-2755>

#### REFERENCES

1. A. Armin, W. Li, O. J. Sandberg, Z. Xiao, L. M. Ding, J. Nelson, D. Neher, K. Vandewal, S. Shoaee, T. Wang, H. Ade, T. Heumüller, C. Brabec, P. Meredith, *Adv. Energy Mater.* **2021**, *11*, 2003570.
2. G. Zhang, F. R. Lin, F. Qi, T. Heumüller, A. Distler, H. J. Egelhaaf, N. Li, P. C. Y. Chow, C. J. Brabec, A. K. Jen, H. L. Yip, *Chem. Rev.* **2022**, *122*, 14180.
3. H. Yao, J. Hou, *Angew. Chem. Int. Ed.* **2022**, *61*, e202209021.
4. J. Hou, O. Inganäs, R. H. Friend, F. Gao, *Nat. Mater.* **2018**, *17*, 119.
5. Z. Zheng, J. Wang, P. Bi, J. Ren, Y. Wang, Y. Yang, X. Liu, S. Zhang, J. Hou, *Joule* **2022**, *6*, 171.
6. Y. Jiang, S. Sun, R. Xu, F. Liu, X. Miao, G. Ran, K. Liu, Y. Yi, W. Zhang, X. Zhu, *Nat. Energy* **2024**, *9*, 975.
7. H. Lu, D. Li, W. Liu, G. Ran, H. Wu, N. Wei, Z. Tang, Y. Liu, W. Zhang, Z. Bo, *Angew. Chem. Int. Ed.* **2024**, *63*, e202407007.
8. M. Ans, A. Ayub, N. Alwadai, A. Rasool, M. Zahid, J. Iqbal, M. S. Al-Buriah, *J. Phys. D: Appl. Phys.* **2022**, *55*, 235501.
9. M. Ans, K. Ayub, S. Muhammad, J. Iqbal, *Comput. Theor. Chem.* **2019**, *1161*, 26.
10. M. Ans, K. Ayub, X. Xiao, J. Iqbal, *J. Mol. Liq.* **2020**, *298*, 111963.
11. M. Ans, J. Iqbal, B. Eliasson, M. J. saif, K. Ayub, *Comput. Mater. Sci.* **2019**, *159*, 150.
12. M. Ans, M. Paramasivam, K. Ayub, R. Ludwig, M. Zahid, X. Xiao, J. Iqbal, *J. Mol. Liq.* **2020**, *305*, 112829.
13. H. Yu, Y. Wang, C. H. Kwok, R. Zhou, Z. Yao, S. Mukherjee, A. Sergeev, H. Hu, Y. Fu, H. M. Ng, L. Chen, D. Zhang, D. Zhao, Z. Zheng, X. Lu, H. Yin, K. S. Wong, H. Ade, C. Zhang, Z. Zhu, H. Yan, *Joule* **2024**, *8*, 2304.
14. H. Yu, Y. Wang, X. Zou, H. Han, H. K. Kim, Z. Yao, Z. Wang, Y. Li, H. M. Ng, W. Zhou, J. Zhang, S. Chen, X. Lu, K. S. Wong, Z. Zhu, H. Yan, H. Hu, *Adv. Funct. Mater.* **2023**, *33*, 2300712.
15. H. Yu, Y. Wang, H. K. Kim, X. Wu, Y. Li, Z. Yao, M. Pan, X. Zou, J. Zhang, S. Chen, D. Zhao, F. Huang, X. Lu, Z. Zhu, H. Yan, *Adv. Mater.* **2022**, *34*, 2200361.
16. J. Nelson, J. J. Kwiatkowski, J. Kirkpatrick, J. M. Frost, *Acc. Chem. Res.* **2009**, *42*, 1768.
17. J. Yi, G. Zhang, H. Yu, H. Yan, *Nat. Rev. Mater.* **2023**, *9*, 46.
18. L. Ye, H. Hu, M. Ghasemi, T. Wang, B. A. Collins, J. H. Kim, K. Jiang, J. H. Carpenter, H. Li, Z. Li, T. McAfee, J. Zhao, X. Chen, J. L. Y. Lai, T. Ma, J. L. Bredas, H. Yan, H. Ade, *Nat. Mater.* **2018**, *17*, 253.
19. G. Han, Y. Yi, Z. Shuai, *Adv. Energy Mater.* **2018**, *8*, 1702743.

20. H. Yu, M. Pan, R. Sun, I. Agunawela, J. Zhang, Y. Li, Z. Qi, H. Han, X. Zou, W. Zhou, S. Chen, J. Y. L. Lai, S. Luo, Z. Luo, D. Zhao, X. Lu, H. Ade, F. Huang, J. Min, H. Yan, *Angew. Chem. Int. Ed.* **2021**, *60*, 10137.
21. Y. Cui, H. Yao, J. Zhang, T. Zhang, Y. Wang, L. Hong, K. Xian, B. Xu, S. Zhang, J. Peng, Z. Wei, F. Gao, J. Hou, *Nat. Commun.* **2019**, *10*, 2515.
22. X. Li, M.-A. Pan, T.-K. Lau, W. Liu, K. Li, N. Yao, F. Shen, S. Huo, F. Zhang, Y. Wu, X. Li, X. Lu, H. Yan, C. Zhan, *Chem. Mater.* **2020**, *32*, 5182.
23. C. Zhu, J. Yuan, F. Cai, L. Meng, H. Zhang, H. Chen, J. Li, B. Qiu, H. Peng, S. Chen, Y. Hu, C. Yang, F. Gao, Y. Zou, Y. Li, *Energy Environ. Sci.* **2020**, *13*, 2459.
24. K. Jiang, Q. Wei, J. Y. L. Lai, Z. Peng, H. K. Kim, J. Yuan, L. Ye, H. Ade, Y. Zou, H. Yan, *Joule* **2019**, *3*, 3020.
25. Y. Yang, Z. Liu, G. Zhang, X. Zhang, D. Zhang, *Adv. Mater.* **2019**, *31*, e1903104.
26. X. Bi, S. Li, T. He, H. Chen, Y. Li, X. Jia, X. Cao, Y. Guo, Y. Yang, W. Ma, Z. Yao, B. Kan, C. Li, X. Wan, Y. Chen, *Small* **2024**, *20*, 2311561.
27. T. Duan, J. Wang, X. Zuo, X. Bi, C. Zhong, Y. Li, Y. Long, K. Tu, W. Zhang, K. Yang, H. Zhou, X. Wan, Y. Zhao, B. Kan, Y. Chen, *Mater. Horiz.* **2024**. <https://doi.org/10.1039/D4MH00699B>
28. H. Yu, C. Zhao, H. Hu, S. Zhu, B. Zou, T. A. Dela Peña, H. M. Ng, C. H. Kwok, J. Yi, W. Liu, M. Li, J. Wu, G. Zhang, Y. Chen, H. Yan, *Energy Environ. Sci.* **2024**, *17*, 5191.
29. B. Zou, H. M. Ng, H. Yu, P. Ding, J. Yao, D. Chen, S. H. Pun, H. Hu, K. Ding, R. Ma, M. Qammar, W. Liu, W. Wu, J. Y. L. Lai, C. Zhao, M. Pan, L. Guo, J. E. Halpert, H. Ade, G. Li, H. Yan, *Adv. Mater.* **2024**, *36*, 2405404.
30. H. Sirringhaus, *Adv. Mater.* **2005**, *17*, 2411.
31. G. Li, V. Shrotriya, J. Huang, Y. Yao, T. Moriarty, K. Emery, Y. Yang, *Nat. Mater.* **2005**, *4*, 864.
32. R. Noriega, J. Rivnay, K. Vandewal, F. P. V. Koch, N. Stingelin, P. Smith, M. F. Toney, A. Salleo, *Nat. Mater.* **2013**, *12*, 1038.
33. H. Chen, Y. Guo, G. Yu, Y. Zhao, J. Zhang, D. Gao, H. Liu, Y. Liu, *Adv. Mater.* **2012**, *24*, 4618.
34. C. Wang, Y. Qin, Y. Sun, Y. S. Guan, W. Xu, D. Zhu, *ACS Appl. Mater. Interfaces* **2015**, *7*, 15978.
35. S. Chen, B. Sun, W. Hong, H. Aziz, Y. Meng, Y. Li, *J. Mater. Chem. C* **2014**, *2*, 2183.
36. C. Zhang, Y. Zang, F. Zhang, Y. Diao, C. R. McNeill, C. A. Di, X. Zhu, D. Zhu, *Adv. Mater.* **2016**, *28*, 8456.
37. M. Hamsch, T. Erdmann, A. R. Chew, S. Bernstorff, A. Salleo, A. Kiriy, B. Voit, S. C. B. Mannsfeld, *J. Mater. Chem. C* **2019**, *7*, 3665.
38. C. Zhu, L. Meng, J. Zhang, S. Qin, W. Lai, B. Qiu, J. Yuan, Y. Wan, W. Huang, Y. Li, *Adv. Mater.* **2021**, *33*, e2100474.
39. J. S. Park, G. U. Kim, D. Lee, S. Lee, B. Ma, S. Cho, B. J. Kim, *Adv. Funct. Mater.* **2020**, *30*, 2005787.
40. Y. Cui, H. Yao, J. Zhang, K. Xian, T. Zhang, L. Hong, Y. Wang, Y. Xu, K. Ma, C. An, C. He, Z. Wei, F. Gao, J. Hou, *Adv. Mater.* **2020**, *32*, 1908205.
41. C. Li, J. Zhou, J. Song, J. Xu, H. Zhang, X. Zhang, J. Guo, L. Zhu, D. Wei, G. Han, J. Min, Y. Zhang, Z. Xie, Y. Yi, H. Yan, F. Gao, F. Liu, Y. Sun, *Nat. Energy* **2021**, *6*, 605.
42. S. Luo, C. Li, J. Zhang, X. Zou, H. Zhao, K. Ding, H. Huang, J. Song, J. Yi, H. Yu, K. S. Wong, G. Zhang, H. Ade, W. Ma, H. Hu, Y. Sun, H. Yan, *Nat. Commun.* **2023**, *14*, 6964.
43. G. Han, X. Shen, R. Duan, H. Geng, Y. Yi, *J. Mater. Chem. C* **2016**, *4*, 4654.
44. N. R. Tummala, Z. Zheng, S. G. Aziz, V. Coropceanu, J.-L. Bredas, *J. Phys. Chem. Lett.* **2015**, *6*, 3657.
45. H. F. Haneef, A. M. Zeidell, O. D. Jurchescu, *J. Mater. Chem. C* **2020**, *8*, 759.
46. A. S. Hassaniien, A. A. Akl, *J. Alloy. Compd.* **2015**, *648*, 280.
47. L. Perdígón-Toro, H. Zhang, A. Markina, J. Yuan, S. M. Hosseini, C. M. Wolff, G. Zuo, M. Stolterfoht, Y. Zou, F. Gao, D. Andrienko, S. Shoaee, D. Neher, *Adv. Mater.* **2020**, *32*, 1906763.
48. S. M. Hosseini, N. Tokmoldin, Y. W. Lee, Y. Zou, H. Y. Woo, D. Neher, S. Shoaee, *Solar RRL* **2020**, *4*, 2000498.
49. T. Wang, V. Coropceanu, J.-L. Brédas, *Chem. Mater.* **2019**, *31*, 6239.
50. M. J. Frisch, G. W. Trucks, H. B. Schlegel, G. E. Scuseria, M. A. Robb, J. R. Cheeseman, G. Scalmani, V. Barone, G. A. Petersson, H. Nakatsuji, X. Li, M. Caricato, A. V. Marenich, J. Bloino, B. G. Janesko, R. Gomperts, B. Mennucci, H. P. Hratchian, J. V. Ortiz, A. F. Izmaylov, J. L. Sonnenberg, Williams, F. Ding, F. Lipparini, F. Egidi, J. Goings, B. Peng, A. Petrone, T. Henderson, D. Ranasinghe, et al, Gaussian 16 Rev. C.01. Wallingford, CT, **2016**.
51. T. Stein, H. Eisenberg, L. Kronik, R. Baer, *Phys. Rev. Lett.* **2010**, *105*, 266802.
52. L. Pandey, C. Doiron, J. S. Sears, J.-L. Brédas, *Phys. Chem. Chem. Phys.* **2012**, *14*, 14243.
53. X. Shen, G. Han, Y. Yi, *Phys. Chem. Chem. Phys.* **2016**, *18*, 15955.
54. B. Hess, C. Kutzner, D. van der Spoel, E. Lindahl, *J. Chem. Theory Comput.* **2008**, *4*, 435.
55. S. Pronk, S. Páll, R. Schulz, P. Larsson, P. Bjelkmar, R. Apostolov, M. R. Shirts, J. C. Smith, P. M. Kasson, D. van der Spoel, B. Hess, E. Lindahl, *Bioinformatics* **2013**, *29*, 845.
56. W. L. Jorgensen, D. S. Maxwell, J. Tirado-Rives, *J. Am. Chem. Soc.* **1996**, *118*, 11225.
57. W. L. Jorgensen, J. Tirado-Rives, *J. Am. Chem. Soc.* **1988**, *110*, 1657.
58. C. I. Bayly, P. Cieplak, W. Cornell, P. A. Kollman, *J. Phys. Chem.* **1993**, *97*, 10269.
59. T. Lu, F. Chen, *J. Comput. Chem.* **2012**, *33*, 580.
60. H. Bässler, *Phys. Stat. Sol.* **1993**, *175*, 15.
61. R. A. Marcus, *J. Chem. Phys.* **1956**, *24*, 966.
62. A. A. Voityuk, N. Rosch, *J. Chem. Phys.* **2002**, *117*, 5607.
63. Z. Cao, S. Yang, B. Wang, X. Shen, G. Han, Y. Yi, *J. Mater. Chem. A* **2020**, *8*, 20408.
64. T. Wang, J. L. Brédas, *Adv. Funct. Mater.* **2019**, *29*, 1806845.
65. J. Zhou, Y. C. Zhou, J. M. Zhao, C. Q. Wu, X. M. Ding, X. Y. Hou, *Phys. Rev. B* **2007**, *75*, 153201.
66. J. J. M. van der Holst, F. W. A. van Oost, R. Coehoorn, P. A. Bobbert, *Phys. Rev. B* **2011**, *83*, 085206.
67. H. Li, Y. Li, H. Li, J. L. Brédas, *Adv. Funct. Mater.* **2017**, *27*, 1605715.
68. M. Andrea, K. Kordos, E. Lidorikis, D. G. Papageorgiou, *Comput. Mater. Sci.* **2022**, *202*, 110978.
69. H. Uratani, S. Kubo, K. Shizu, F. Suzuki, T. Fukushima, H. Kaji, *Sci. Rep.* **2016**, *6*, 39128.
70. J. Ho, A. Klamt, M. L. Coote, *J. Phys. Chem. A* **2010**, *114*, 13442.

## SUPPORTING INFORMATION

Additional supporting information can be found online in the Supporting Information section at the end of this article.

**How to cite this article:** R. Zhou, C. Li, Z. Wen, C. Zhang, Y. Shi, H. Hou, X. Chen, Q. Kang, Y. Zhang, H. Yan, H. Yu, Y. Zhao, Z. Zheng, H. Yan, *Aggregate* **2025**, *6*, e664. <https://doi.org/10.1002/agt2.664>